

# Autonomous Sorting of Beads in a 3D Environment Using Levitating Magnetic Microrobots

Franco N. Piñan Basualdo,\* Corrado Verde, Fanny Ficuciello, and Sarthak Misra

This work presents a novel approach to autonomously sort passive beads in 3D environments using an untethered levitating magnetic microrobot. The in situ untethered magnetic weighing technique is introduced, where the classification of beads is based on the magnetic force required to levitate the microrobot and the beads. Autonomous sorting is achieved through the integration of motion control, trajectory planning, and action scheduling. Experimental validation is conducted using a nine-coil electromagnetic actuation system and a microrobot of 3 mm in size. The system demonstrates an average trajectory-following precision of 0.1 mm. The proposed magnetic weighing enables the detection and classification of carried silica beads of 0.75–1.00 mm diameter by measuring the increase in effective weight with a resolution of  $\approx 1 \mu\text{N}$ . During the sorting process, all particles with a diameter larger than 0.9 mm are classified as heavy, and all those with a diameter smaller than 0.85 mm are classified as light, demonstrating the effectiveness of the approach. Overall, the proposed system holds significant promise for applications in biomedicine and micromanufacturing, driving innovation in autonomous microrobotics.

biomedical studies conducted on clusters ( $<1 \text{ mm}$ ) or individual cells ( $1\text{--}100 \mu\text{m}$ ) require effective classification and sorting methods. Traditionally, these operations have relied on manual intervention by trained operators using microscopes and pipettes for sorting, which can be labor-intensive. To address this challenge, various approaches have been developed to enable automated or semi-automated sorting of small samples for applications in micro-assembly<sup>[1]</sup> and biology.<sup>[2]</sup> These techniques can be broadly categorized into batch and individual sorting systems. In the following discussion, throughput will be used as the main axis of comparison, as accuracy is not consistently reported across studies, and its requirements can vary significantly depending on the application. Despite the inherent trade-off between throughput and accuracy, the throughput values provided here are not

## 1. Introduction

The ongoing trend toward miniaturization in technology has motivated the advancement of manipulation and sorting techniques specifically designed for small-scale objects. For example,

normalized, and establishing a standardized evaluation framework remains an open research challenge.


Batch sorting techniques involve sorting multiple particles simultaneously by exploiting some physical separation phenomena. At small scales, most batch sorting techniques rely on microfluidic devices,<sup>[3]</sup> where particles can be sorted by size, weight, or stiffness, exploiting their passive separation in fluid flows.<sup>[4]</sup> For example, cells can be passively separated by shape<sup>[5]</sup> or stiffness.<sup>[6]</sup> Alternatively, various active techniques provided enhanced control within microfluidic chips. Acoustic actuation, for instance, can effectively sort cells<sup>[7]</sup> and microspheres.<sup>[8]</sup> Dielectrophoresis, utilizing electric fields to manipulate particles, has been employed to sort cells<sup>[9]</sup> and micro-sized objects.<sup>[10]</sup> Additionally, magnetic forces have been utilized for sorting magnetic particles<sup>[11]</sup> and cells previously labeled with magnetic materials.<sup>[12]</sup> Although batch techniques normally offer high throughput ( $>1000$  particles per second) and purity ( $>90\%$ ),<sup>[13]</sup> their implementation requires circulating all the samples through the separation mechanism, which might be ineffective in some scenarios. For example, when a few samples need to be removed from a large batch, circulating all samples can risk damaging the others. Therefore, individual sensing and sorting can be beneficial in these scenarios.

Individual sorting techniques classify and sort particles one at a time without disturbing the other samples. These sorting techniques can be further classified into tethered and untethered solutions.

F. N. Piñan Basualdo, C. Verde, S. Misra  
Surgical Robotics Laboratory  
Department of Biomechanical Engineering  
University of Twente  
7522 NB Enschede, The Netherlands  
E-mail: f.n.pinanbasualdo@utwente.nl

C. Verde, F. Ficuciello  
ICAROS and PRISMA Laboratories  
Department of Electrical Engineering and Information Technology  
University of Naples Federico II  
80131 Naples, Italy

S. Misra  
Surgical Robotics Laboratory  
Department of Biomaterials and Biomedical Technology  
University of Groningen and University Medical Centre Groningen  
9713 GZ Groningen, The Netherlands

 The ORCID identification number(s) for the author(s) of this article can be found under <https://doi.org/10.1002/aisy.202500200>.

© 2025 The Author(s). Advanced Intelligent Systems published by Wiley-VCH GmbH. This is an open access article under the terms of the Creative Commons Attribution License, which permits use, distribution and reproduction in any medium, provided the original work is properly cited.

DOI: 10.1002/aisy.202500200

Tethered sorting techniques use mechanical tools, such as robotic arms, to pick and sort individual particles. These solutions rely on additional information, such as visual or electrical measurements, to classify particles before sorting them. For example, a robotic arm equipped with a pipette has been utilized to sort zebrafish embryos that had previously been classified based on visual information.<sup>[14]</sup> Capillary adhesion has been exploited to grasp glass beads that had been electrostatically arranged.<sup>[1]</sup> A vacuum gripper has been utilized to sort microspheres and zebrafish eggs.<sup>[15]</sup> Tethered methods can provide intermediate throughput ( $\approx 1$ – $10$  samples per second),<sup>[16]</sup> with an accuracy that depends on the classification technique and can attain 95% for visual methods.<sup>[14]</sup> Nevertheless, tethered solutions require open access to the sample environment, preventing their use in enclosed locations.

Untethered sorting tools, in contrast, utilize externally controlled microrobots to sort particles in difficult-to-reach or enclosed environments.<sup>[17]</sup> Microrobotic sorting is achieved either by directly manipulating the particles to sort or by controlling microrobots that, in turn, manipulate the particles. For example, optical tweezers can directly actuate the particles<sup>[18,19]</sup> or control intermediate structures when the particles are not suitable for optical trapping.<sup>[20,21]</sup> Similarly, laser-powered thermocapillary flows can actuate particles directly<sup>[22]</sup> or steer bubbles that actuate particles.<sup>[23]</sup> Alternatively, untethered soft magnetic microrobots have been used to manipulate nonmagnetic objects in 2D<sup>[24,25]</sup> or 3D<sup>[26–28]</sup> spaces by acting as untethered microrobots. Similarly, collectives of magnetic microrobots can manipulate particles in 2D<sup>[29,30]</sup> or 3D<sup>[31]</sup> environments by exploiting the interactions between the microrobots. Regarding perception, microrobots can integrate sensors for the collection of local measurements.<sup>[32]</sup> For example, miniature strain sensors can be integrated onto microrobots to measure forces.<sup>[33,34]</sup> Untethered microrobotic sorting offers the lowest throughput ( $< 0.1$  samples per second). Nevertheless, its ability to operate in enclosed environments helps minimize sample contamination,<sup>[35]</sup> thus making it particularly suitable for handling sensitive samples in sterile conditions. Despite these opportunities, untethered microrobotic sorting currently depends on manual operation by qualified users, posing challenges for automation and large-scale deployment.

In that context, we propose the use of a levitating magnetic microrobot in the shape of a cup (shown in **Figure 1**) to autonomously sort passive beads in a 3D environment, integrating in situ weighing for classification. To classify the beads, we

propose to adapt magnetic weighing techniques to our freely levitating untethered microrobot. The proposed untethered magnetic weighing consists of estimating the particles' effective weight by the required magnetic force to keep the microrobot levitating in the same place. Unlike traditional magnetic weighing that structurally constrains the motion,<sup>[36]</sup> our system relies on active magnetic stabilization in the three directions. Additionally, low-level control and high-level motion planning are developed to achieve a fully automated microrobotic sorting system. The proposed approach is experimentally validated in a nine-coil electromagnetic actuation system, where silica beads of 0.75– $1.00$  mm diameter were sorted into light and heavy categories. In our experiments, all particles with diameters larger than  $0.9$  mm were consistently classified as heavy, while those smaller than  $0.85$  mm were classified as light, demonstrating the effectiveness of the proposed microrobotic sorting method.

## 2. Proposal

This work aims to develop a microrobotic tool to autonomously sort passive beads by weight by picking them from an initial deposit and depositing them in the appropriate target. For this, we propose to use a magnetic microrobot, shown in **Figure 1**, designed to collect, transport, classify, and release the passive beads. Planning and control algorithms are developed to perform these operations autonomously. In this section, the dynamics of the system are analyzed, and the proposed low- and high-level control strategies are presented.

### 2.1. System Dynamics

As a first step toward the development of a magnetic microrobotic tool, we analyze the dynamics of magnetic control in a 3D space. A magnetic object in a magnetic field ( $\mathbf{B} \in \mathbb{R}^3$ ) experiences a torque ( $\boldsymbol{\tau}_{\text{mag}} \in \mathbb{R}^3$ ) and a force ( $\mathbf{F}_{\text{mag}} \in \mathbb{R}^3$ ), as shown in **Figure 2A**. If we model the magnet as a point dipole, then we can write

$$\begin{aligned}\boldsymbol{\tau}_{\text{mag}} &= \mathbf{m} \times \mathbf{B} \\ \mathbf{F}_{\text{mag}} &= (\mathbf{m} \cdot \nabla) \mathbf{B}\end{aligned}\quad (1)$$

where  $\mathbf{m} \in \mathbb{R}^3$  is the magnetic dipole moment. For permanent magnets, the magnetic moment can be computed as  $\mathbf{m} = V\mathbf{B}_r/\mu_0$ , where  $V \in \mathbb{R}$  is the magnet volume,  $\mu_0 \in \mathbb{R}$  is

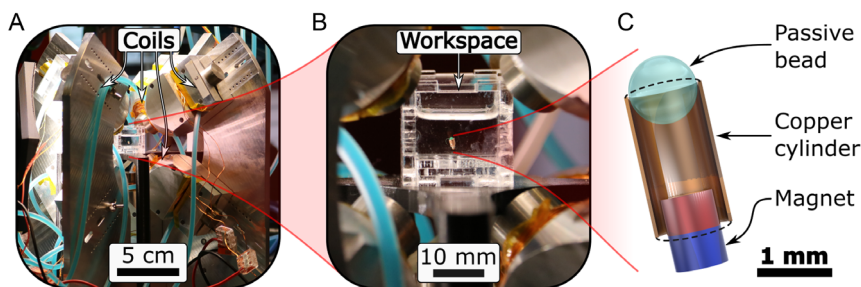


**Figure 1.** Magnetic actuation system and microrobot. A) Water-cooled nine-coil magnetic actuation system and cube workspace. B) Magnetic microrobot levitating while holding a passive green bead. C) Composition of the microrobot.

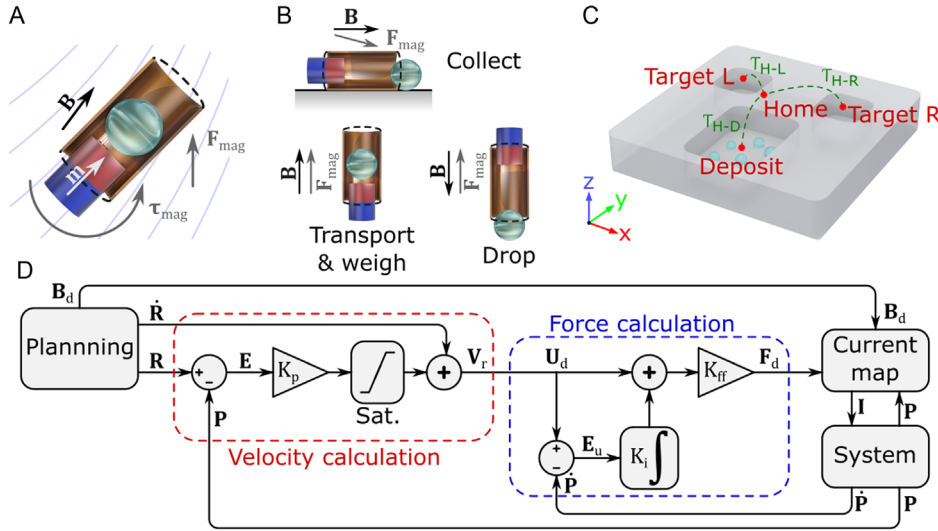


**Figure 2.** System dynamics and control. A) Magnetic untethered actuation. The magnet can be modeled as a point dipole ( $\mathbf{m}$ ) in a magnetic field ( $\mathbf{B}$ ). The magnet will experience a magnetic torque ( $\tau_{\text{mag}}$ ), which will tend to align the magnet with the magnetic field ( $\mathbf{B}$ ), and a magnetic force ( $\mathbf{F}_{\text{mag}}$ ) in the direction of the magnetic gradient. B) The different operations that can be performed are collect, transport, and drop. The different operations require independent orientation and force control. C) Trajectory planning between the home position and the deposit ( $T_{H-D}$ ), and the left and right targets ( $T_{H-L}$  and  $T_{H-R}$ , respectively). A smooth, collision-free trajectory is found by first finding a feasible path and then interpolating to define the reference time sequence. D) Low-level trajectory-following controller diagram. First, a reference velocity to follow the trajectory is defined. Then, the necessary force is computed with an integral action to compensate for modeling errors and noise.

the vacuum magnetic permeability, and  $\mathbf{B}_r \in \mathbb{R}^3$  is the magnetic remanence. Notice that this dipole model predicts a magnetic torque ( $\tau_{\text{mag}}$ ) perpendicular to the magnetic moment ( $\mathbf{m}$ ), thus resulting in the rotation around the magnetization direction being uncontrolled. Consequently, our microrobot is designed to be symmetric around the magnetization axis, mitigating the influence of uncontrolled rotations.

To analyze the response of the microrobot to magnetic torques and forces, we construct its dynamic model considering gravity, viscous drag, and the magnetic effects in Equation (1). For the low Reynolds number regime, the drag force and torque can be described by Faxén's law,<sup>[37]</sup> and the system rotation and translation dynamics can be written as

$$\begin{aligned} I\dot{\omega} + b_R\omega &= \mathbf{m} \times \mathbf{B} \\ m\ddot{\mathbf{P}} + b_T\dot{\mathbf{P}} &= (\mathbf{m} \cdot \nabla)\mathbf{B} + \mathbf{W}_{\text{eff}} \end{aligned} \quad (2)$$

where  $I \in \mathbb{R}_{>0}$  and  $m \in \mathbb{R}_{>0}$  are the magnet's moment of inertia and mass, respectively;  $\omega \in \mathbb{R}^3$  is the angular velocity;  $\mathbf{P} \in \mathbb{R}^3$  is the magnet position;  $b_R \in \mathbb{R}_{>0}$  and  $b_T \in \mathbb{R}_{>0}$  are the rotation and translation viscous drag, respectively; and  $\mathbf{W}_{\text{eff}} \in \mathbb{R}^3$  is the magnet's effective weight (considering buoyancy). At the submillimeter scale, it is often possible to neglect the rotation dynamics ( $I\dot{\omega} + b_R\omega \approx \mathbf{0}$ ) and assume the magnet to be instantaneously aligned with the applied field.<sup>[38]</sup> Similarly, the translational inertia can be neglected ( $m\ddot{\mathbf{P}} \approx \mathbf{0}$ ), thus simplifying Equation (2) to

$$\begin{aligned} \mathbf{m} &= \|\mathbf{m}\|\hat{\mathbf{B}} \\ b_T\dot{\mathbf{P}} &= (\mathbf{m} \cdot \nabla)\mathbf{B} + \mathbf{W}_{\text{eff}} \end{aligned} \quad (3)$$

where  $\hat{\mathbf{B}} = \mathbf{B}/\|\mathbf{B}\|$  is the unit vector in the direction of the field. For a validation of these assumptions, see Supporting

Information. In this case, the orientation and position of the magnet can be controlled through the magnetic field and gradient, respectively.

## 2.2. Magnetic Actuation

To control the magnetic microrobot, we must control the magnetic field and the gradient around it. A way to create and control magnetic fields is to use multiple electromagnetic coils around the workspace. The magnetic field created by multiple coils (whose cores are not saturated) is the linear combination of the fields created by each coil. In that case, we can write

$$\mathbf{B}(\mathbf{P}, \mathbf{I}) = \mathcal{B}(\mathbf{P})\mathbf{I} \quad (4)$$

where  $\mathcal{B} \in \mathbb{R}^{3 \times n}$  is the characteristic field matrix, and  $\mathbf{I} \in \mathbb{R}^n$  is the current vector of a magnetic actuation system with  $n \in \mathbb{N}$  coils. Furthermore, using Equation (4), we can rewrite the magnetic force ( $\mathbf{F}_{\text{mag}}$ ) as

$$\mathbf{F}_{\text{mag}}(\mathbf{P}, \mathbf{I}) = \underbrace{\begin{pmatrix} \mathbf{m}^T \mathcal{B}_x(\mathbf{P}) \\ \mathbf{m}^T \mathcal{B}_y(\mathbf{P}) \\ \mathbf{m}^T \mathcal{B}_z(\mathbf{P}) \end{pmatrix}}_{\mathcal{F}(\mathbf{P}, \mathbf{m})} \mathbf{I} \quad (5)$$

where  $\mathcal{B}_k = \frac{\partial \mathcal{B}}{\partial k} \in \mathbb{R}^{3 \times n}$  are the derivatives of  $\mathcal{B}$  (for  $k = x, y, z$ ), and  $\mathcal{F} \in \mathbb{R}^{3 \times n}$  is the characteristic force matrix of a magnetic actuation system with  $n$  coils. Additionally, Equation (3) enables the computation of  $\mathcal{F}$  assuming the magnet will be aligned with the applied field ( $\mathbf{m} = \|\mathbf{m}\|\hat{\mathbf{B}}_d$ ).

The objective of the control algorithm is to find the set of currents ( $\mathbf{I}_d \in \mathbb{R}^n$ ) that would give place to the desired field

( $\mathbf{B}_d \in \mathbb{R}^3$ ) and force ( $\mathbf{F}_d \in \mathbb{R}^3$ ). Although numerical optimization techniques can be used to solve general pose control problems,<sup>[39]</sup> in this case, the dynamic system is linear

$$\underbrace{\begin{pmatrix} \mathbf{B}_d \\ \mathbf{F}_d \end{pmatrix}}_{\mathbf{S}_d} = \underbrace{\begin{pmatrix} \mathcal{B}(\mathbf{P}) \\ \mathcal{F}(\mathbf{P}, \|\mathbf{m}\| \hat{\mathbf{B}}_d) \end{pmatrix}}_{\mathcal{S}(\mathbf{P}, \|\mathbf{m}\| \hat{\mathbf{B}}_d)} \mathbf{I}_d \quad (6)$$

where  $\mathbf{S}_d \in \mathbb{R}^6$  is the desired input (field and force), and  $\mathcal{S} \in \mathbb{R}^{6 \times n}$  is the total system matrix. For systems with  $n > 6$  coils, Equation (6) is underdetermined. In that case, the system is solved by finding the Moore–Penrose inverse matrix ( $\mathcal{S}^+ \in \mathbb{R}^{n \times 6}$ ), which can be used to find a solution as  $\mathbf{I}_d = \mathcal{S}^+ \mathbf{S}_d$ . Moreover, the solution found through the Moore–Penrose inverse matrix minimizes  $\|\mathbf{I}_d\|$ , thus minimizing the total electric power.

### 2.3. Motion Control

Once the dynamics and actuation are modeled, a motion control algorithm is developed. The objective of this low-level controller is to drive the microrobot to follow a reference trajectory  $\mathbf{R}(t)$  (and velocity  $\dot{\mathbf{R}}(t)$ ). Given the system dynamics [Equation (3)], we propose a nested control loop that first computes a control velocity ( $\mathbf{U}_d \in \mathbb{R}^3$ ) to follow the trajectory, and then the control force ( $\mathbf{F}_d$ ) to obtain said velocity, as shown in Figure 2D. The control law can be written as

$$\begin{aligned} \mathbf{U}_d &= \dot{\mathbf{R}} + K_p(\mathbf{R} - \mathbf{P}) \\ \mathbf{F}_d &= K_{ff} \left( \mathbf{U}_d + K_i \int_0^t (\mathbf{U}_d - \dot{\mathbf{P}}) dt \right) - \mathbf{W}_{eff} \end{aligned} \quad (7)$$

where  $K_p \in \mathbb{R}$ , and  $K_i \in \mathbb{R}$  are control parameters. The control velocity ( $\mathbf{U}_d \in \mathbb{R}^3$ ) is computed to asymptotically approach the reference, and the integral action is designed to compensate for disturbances or model errors. Under this applied magnetic force and for  $K_{ff} = b_T$ , the displacement dynamics of the system in Equation (3) simplify to

$$\dot{\mathbf{E}} = -K_p \mathbf{E} - K_i (\mathbf{E} - \mathbf{E}_0) - K_p K_i \int_0^t \mathbf{E} \quad (8)$$

where  $\mathbf{E} = \mathbf{R} - \mathbf{P}$  and  $\mathbf{E}_0 = \mathbf{E}(t = 0)$ . The dynamic system in Equation (8) is stable and will converge to  $\mathbf{E} = \mathbf{0}$  for  $K_p > 0$  and  $K_i > 0$ . However, in practice, deviations between the applied and desired forces due to modeling errors and spatial variations in the magnetic force (see Supporting Information for an estimation of these variations) may introduce perturbations that could affect system stability.

### 2.4. Manipulation and Weighing of Beads

Once the motion control system is developed, the next step is devising strategies for the manipulation and sorting of the beads. The operations that the microrobot should perform are collecting, transporting, weighing, and dropping the passive beads, as shown in Figure 2C. To collect a bead, the microrobot is oriented horizontally, and a downward and horizontal force is applied to press against the bottom while sliding on it. In response, the microrobot moves laterally toward one of the walls while keeping in contact with the bottom of the deposit. During its advancement, the microrobot has a chance to trap a passive bead inside the cup. Although bead collection is inherently stochastic, the system can detect a failed collection during the subsequent weighing step, where the absence of an expected weight increase indicates a failed collection (see **Algorithm 1**). Transport of the beads is achieved by maintaining the cup pointing upwards by imposing an upwards magnetic field ( $\mathbf{B}_d = B_d \hat{\mathbf{z}}$ ) and a levitating magnetic force. Dropping a bead is achieved by inverting the magnetic field ( $\mathbf{B}_d = -B_d \hat{\mathbf{z}}$ ) while levitating the microrobot, letting the bead fall by gravity.

Additionally, the ensemble (microrobot plus carried object) can be weighed by the necessary magnetic force to levitate it. Indeed, in equilibrium ( $\dot{\mathbf{P}} = \mathbf{0}$ ), the magnetic force and effective weight compensate each other ( $\mathbf{F}_{mag} = -\mathbf{W}_{eff}$ ), as shown in Equation (2). This magnetic weighing enables the automation of the sorting process since it allows the in situ classification

**Algorithm 1.** Actions and movements scheduling. The estimated weight ( $W$ ) is compared with the thresholds  $W_{thrH}$  and  $W_{thrL}$  to determine if a heavy, light, or no bead is carried. The colors indicate **Locations**, **Actions**, or **Trajectories**.

---

```

nsorted ← 0
move to Home
while nsorted < nobjective do
    move to Deposit following  $\mathcal{T}_{H-D}$ 
    perform Collect
    move to Home following  $\mathcal{T}_{H-D}^{-1}$ 
    perform Weigh →  $W$ 
    if  $W < W_{thrL}$  then
        continue
    else if  $W > W_{thrH}$  then
        move to Target R following  $\mathcal{T}_{H-R}$ 
        perform Drop R
        move to Home following  $\mathcal{T}_{H-R}^{-1}$ 
    else
        move to Target L following  $\mathcal{T}_{H-L}$ 
        perform Drop L
        move to Home following  $\mathcal{T}_{H-L}^{-1}$ 
    nsorted + 1

```

---

▷ Without prescribed trajectory  
 ▷ No bead is carried, try collecting again.  
 ▷ Heavy bead is carried, drop right.  
 ▷ Light bead is carried, drop left.

---



of the beads. Moreover, magnetic weighing enables the classification of particles of similar sizes but different densities, which can be difficult to visually classify, and it can be more sensitive than methods based on the bead diameter (for example, a 5% change in diameter corresponds to a 16% increase in weight).

## 2.5. Trajectory Planning

Next, the microrobot should safely navigate the workspace. For this, a collision-free trajectory between the reference points (home, deposit, and targets) is computed as shown in Figure 2C. The algorithm consists of first finding a collision-free path between the relevant sites (deposit, home, and targets) in the workspace and then computing the reference time sequence (i.e.,  $\mathbf{R}(t) \in \mathbb{R}^3$ ) to follow the path. Since the relevant sites in the workspace do not change during the procedure, the trajectory planning is performed offline and only between the home position and the three other sites.

The path-finding is performed using a bidirectional rapidly exploring random tree (BiRRT) algorithm.<sup>[40]</sup> This algorithm produces a sequence of sparse points between the initial and target locations that define a collision-free path. However, this path is not smooth and does not take into account the dynamics of the microrobot. Therefore, the found path is interpolated to compute the reference time sequence using a piecewise cubic Hermite interpolating polynomial (PCHIP) algorithm.<sup>[41]</sup> This algorithm produces smooth trajectories (without abrupt changes in velocities) that traverse the found path with a prescribed maximum velocity. This results in planned trajectories ( $\mathcal{T} = \mathbf{R}_T(t) | t \in [0, t_f]$ ) that can also be traversed in the reverse direction ( $\mathcal{T}^{-1} = \mathbf{R}_{T^{-1}}(t) = \mathbf{R}_T(t_f - t) | t \in [0, t_f]$ ). The three planned trajectories are:  $\mathcal{T}_{H-D}$  between the home position and the deposit,  $\mathcal{T}_{H-R}$  between the home position and the right target,  $\mathcal{T}_{H-L}$  between the home position and the left target, as shown in Figure 2C.

## 2.6. Actions Scheduling

The final necessary step toward the autonomous sorting of beads is the implementation of a higher-level logic. This logic, detailed in Algorithm 1, determines the sequence of actions to be performed to achieve autonomous sorting. The initial movement from the arbitrary initial position to the home position ( $\mathbf{P}_H \in \mathbb{R}^3$ ) is performed utilizing the control law described in Equation (7) with a constant reference ( $\mathbf{R} = \mathbf{P}_H$ ,  $\dot{\mathbf{R}} = \mathbf{0}$ ). Then, the sorting is achieved by sequentially collecting, weighing, classifying, and dropping the beads. All the subsequent movements between the home position and the deposit or target points are performed following the trajectories computed previously.

## 3. Results

The proposed approach is experimentally validated in a nine-coil electromagnetic actuation system where the microrobot autonomously sorts silica beads of 0.75–1.00 mm diameter into two categories, heavy and light beads.

### 3.1. Trajectory Planning and Following

The trajectory planning algorithm proposed in the previous section is used to find the reference time sequence to drive the microrobot from the home position to the deposit and both targets. The algorithm, consisting of a BiRRT path planning followed by a PCHIP interpolation, results in a smooth trajectory, as shown in Figure 3A,B, where the maximum reference velocity is  $\|\dot{\mathbf{R}}\| \leq 0.4 \text{ mm s}^{-1}$ . Notice that the proposed algorithm ensures smooth profiles and that the trajectories start and end with zero velocity.

Then, the trajectory-following is validated experimentally with an empty microrobot in the vertical orientation. The control parameters are set to  $K_p = K_i = 2 \text{ s}^{-1}$  and  $K_{ff} = 9 \mu\text{N} (\text{mm s}^{-1})^{-1}$ . Starting at an arbitrary position at the bottom of the workspace, the microrobot is first taken to the home position ( $\mathbf{P}_H$ ) without a prescribed trajectory. Then, the microrobot is commanded to follow the planned trajectories (in both directions) in the following order:  $\mathcal{T}_{H-D}$ ,  $\mathcal{T}_{H-R}$ ,  $\mathcal{T}_{H-D}$ , and  $\mathcal{T}_{H-L}$ . The microrobot stops for 6 s in each target position to simulate performing some operation. The results are shown in Figure 3C,D, where the mean and maximum errors after the initial approach are 0.1 and 0.4 mm, respectively.

### 3.2. Magnetic Weighing

To validate the proposed magnetic weighing and classification strategy, the required magnetic forces to levitate the empty and loaded microrobot are measured. Each measurement consists of levitating the microrobot at the home position ( $\mathbf{P}_H$ ) using the control law in Equation (7) with a constant reference ( $\mathbf{R} = \mathbf{P}_H$ ,  $\dot{\mathbf{R}} = \mathbf{0}$ ). After stabilization, the required levitation force is measured over 10 s (100 samples) to compute the mean and standard deviation. Two independent measurements are performed in the empty case, resulting in a required levitation force of  $38 \pm 1 \mu\text{N}$ . These results are used to estimate the resolution of the magnetic weighing system to  $\approx 1 \mu\text{N}$ , which is comparable to existing force-sensing microrobots based on strain gauges with a resolution of  $1.5 \mu\text{N}$ .<sup>[33]</sup>

Then, 10 independent measurements with different beads are performed in the loaded case, obtaining a required levitation force of  $45 \pm 3 \mu\text{N}$ . The average bead mass was independently measured using a Secura precision balance (Sartorius Lab Instruments, Germany), yielding 1.0(2) mg. Considering the glass density of  $2500 \text{ kg m}^{-3}$  and the density of silicone oil of  $980 \text{ kg m}^{-3}$ , this corresponds to an effective weight of  $6 \pm 1 \mu\text{N}$  in the fluid, in agreement with the values obtained by the levitating microrobot. For autonomous sorting, a threshold of  $W_{\text{thrL}} = 40.5 \mu\text{N}$  is established to identify if a bead is carried, and a threshold of  $W_{\text{thrH}} = 44.5 \mu\text{N}$  is set to determine if the carried bead is to be considered light or heavy, as shown in Figure 4D.

### 3.3. Autonomous Sorting

Finally, the capabilities of the microrobot and the actuation system to follow the prescribed trajectories and weigh the carried beads are exploited to sort passive beads autonomously. The

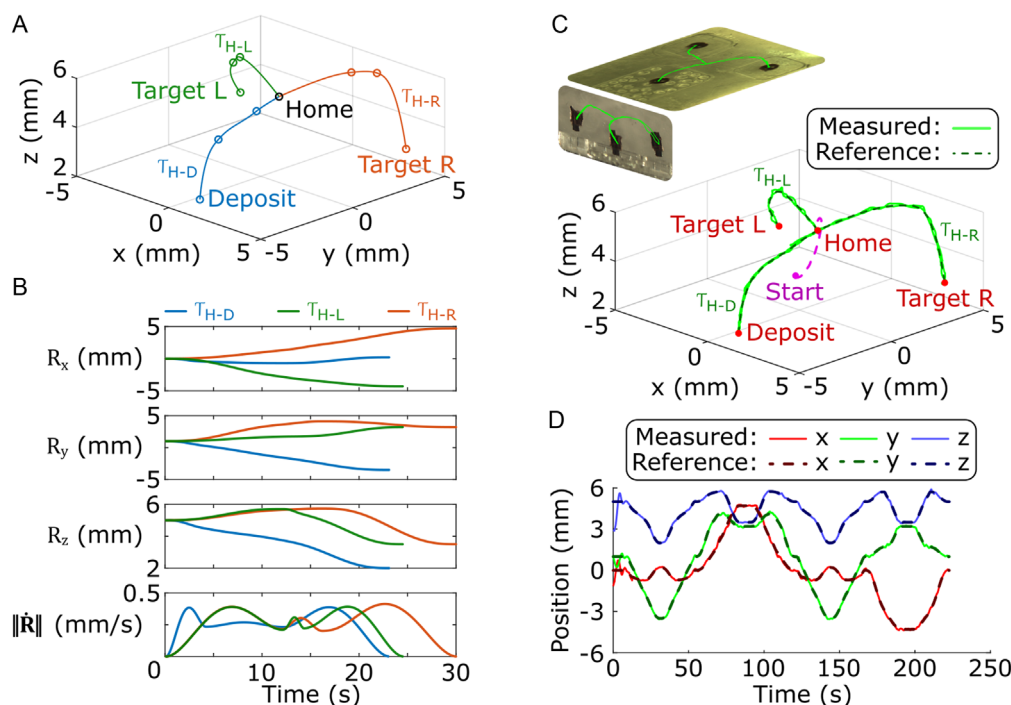


**Figure 3.** Trajectory planning and following results. A) Planned trajectories ( $T_{H-D}$ ,  $T_{H-R}$  and  $T_{H-L}$ ). The paths found by the BiRRT algorithm are represented by circles, and the interpolated trajectories are represented by lines. B) Reference time sequence computed by interpolating the path using a PCHIP algorithm. All the trajectories are smooth and start and finish with zero velocity. C) Experimental trajectory following of an empty microrobot in M1000 silicone oil using the control law in Equation (7) with  $K_p = K_i = 2 \text{ s}^{-1}$  and  $K_{ff} = 9 \mu\text{N} (\text{mm s}^{-1})^{-1}$ . The top and side motion composite images of the experiment are shown as an inset. D) Time evolution of the measured and reference trajectory components. After the initial approach, the mean and maximum errors are 0.1 mm and 0.4 mm, respectively. Refer to Supplementary Video 1, Supporting Information for the recording, and to Figure S5, Supporting Information for the evolution of the control variables.

action scheduling proposed in the algorithm is experimentally validated by sorting glass beads, as shown in Figure 4A,B. Starting from the home position, the microrobot first attempts to collect a bead from the deposit. Then, the weight of the ensemble ( $W$ ) is estimated by averaging the required levitation force over 100 time steps (10 s). If the weight estimation suggests that no bead is carried ( $W < W_{\text{thrL}}$ ), the microrobot tries to collect a bead again. Otherwise, the bead is taken and dropped at the corresponding target location (left if  $W_{\text{thrL}} \leq W \leq W_{\text{thrH}}$ , right if  $W > W_{\text{thrH}}$ ). Since the passive beads are not tracked, the collection remains a stochastic process, becoming less effective when the deposit is less crowded. For example, eight attempts were made to collect the fourth particle in the experiment, as shown in Supplementary Video 3, Supporting Information. Nevertheless, the system is capable of detecting a failed collection operation and performing another attempt without interfering with the sorting process.

To assess the sorting efficiency, the diameter of the glass beads before and after the sorting is measured. Combining the results after multiple experiments, the beads in the deposit ( $0.86 \pm 9 \text{ mm}$  diameter) are classified into the left ( $0.80 \pm 5 \text{ mm}$  diameter) and right ( $0.93 \pm 4 \text{ mm}$  diameter) targets, as shown in Figure 4C. The beads dropped at the right target are, on average, 15% larger than the ones dropped at the left target. Moreover, all beads with a diameter larger than 0.90 mm were classified as heavy, while all beads smaller than 0.85 mm were classified as light.

### 3.4. Manipulation in Complex Fluid

To demonstrate the versatility of the proposed strategy, a collection, weighing, and drop operation is performed in a 2.5% w/v sodium carboxymethyl cellulose (CMC) in water. This solution will have a viscosity of  $\approx 1 \text{ Pa s}^{[42]}$  but possesses non-Newtonian viscoelastic properties.<sup>[43]</sup> The performance of the microrobot, shown in Figure 4E, is unhindered by the complex rheology of the media, with the exception that a longer waiting time is necessary to drop the bead.

## 4. Discussion

This work introduces a novel approach to autonomously sort passive beads in 3D environments using a rigid magnetic microrobot. By integrating a solid magnet into a microrobot, we have demonstrated levitation and control of the microrobot with sub-millimeter precision. To classify the beads, we implemented untethered magnetic weighing, consisting of stabilizing the levitating microrobot and estimating the particles' effective weight by the required magnetic force to levitate the ensemble. Then, motion control, trajectory planning, and action scheduling were developed to enable efficient and repetitive sorting operations without the need for user intervention. The proposed approach is validated through the experimental sorting of silica beads by

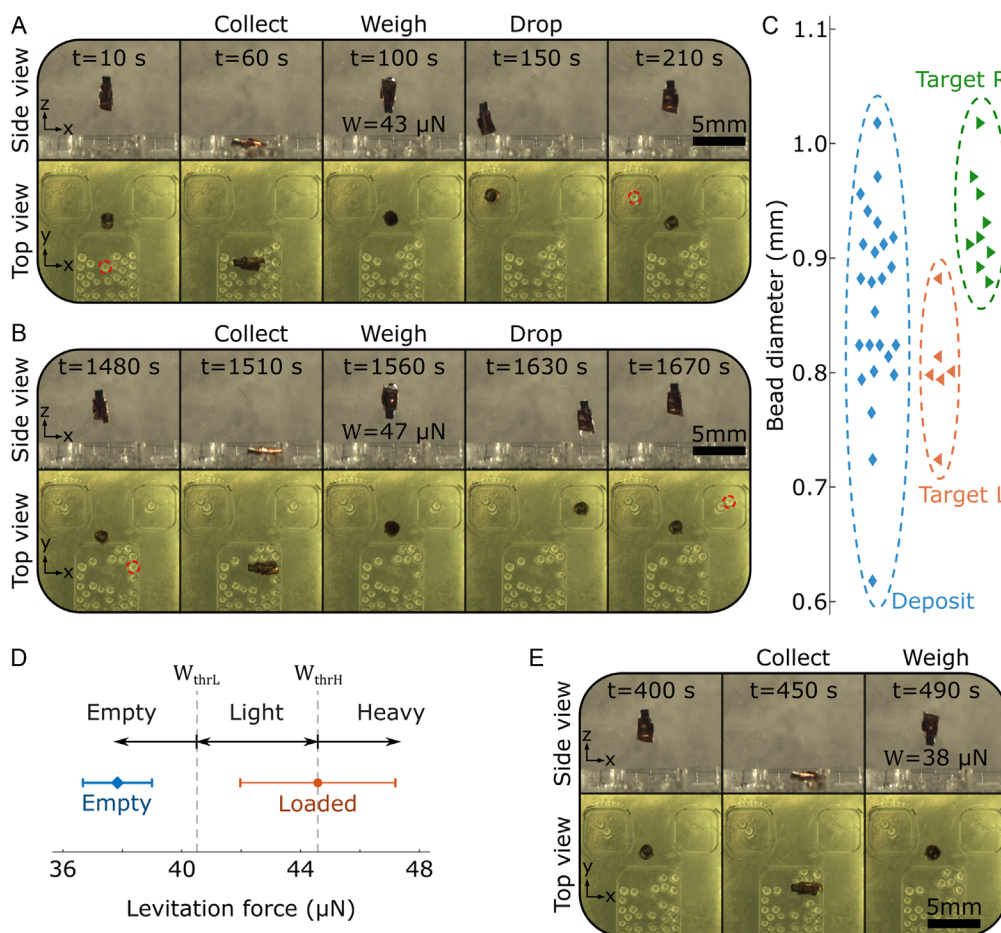


**Figure 4.** Experimental autonomous sorting of glass beads by weight. Collection, weighing, and dropping of a light bead ( $W = 43 \mu\text{N}$ ) A), and a heavy bead ( $W = 47 \mu\text{N}$ ) B). The initial and final positions of the beads are highlighted. C) The measured diameter of the beads before and after sorting (data collected across multiple experiments). The average size difference confirms that the system successfully classifies beads by weight. Refer to Supplementary Video 2, Supporting Information for the recording, and to Figure S6, Supporting Information for the evolution of the control variables. D) Experimental magnetic weighing results. The thresholds to consider a heavy or light bead are defined as  $W_{\text{thrH}} = 44.5 \mu\text{N}$  and  $W_{\text{thrL}} = 40.5 \mu\text{N}$ , respectively. E) Experimental weighing and dropping of a glass bead in a solution of 2.5% w/v of sodium CMC in water. The waiting time during the drop operation was increased with respect to the experiment in silicone oil. Refer to Supplementary Video 3, Supporting Information for the recording.

classifying them into heavy and light categories. The experimental resolution of the proposed untethered magnetic weighing is  $1 \mu\text{N}$ . After the sorting, the diameters of the beads in the heavy and light targets are  $0.93 \pm 4$  and  $0.80 \pm 5$  mm, respectively, showing a 15% difference in size. The resolution of the sorting system is around  $0.05$  mm since all beads with a diameter larger than  $0.90$  mm were classified as heavy, while all beads smaller than  $0.85$  mm were classified as light.

Despite these promising results, the system still suffers from some limitations. First, particles with a density similar to that of the fluid might be difficult to classify due to the limited weighing resolution. One factor limiting weighing resolution is the spatial variation of the magnetic forces, which introduces variations due to errors in the microrobot tracking, as explained in the Supporting Information. A potential solution would be the incorporation of a Maxwell coil to generate a highly homogeneous levitating force, using the remaining coils solely for stabilizing the microrobot in the horizontal directions. Another way to enhance

the weighing resolution is to decrease the effective weight of the microrobot by, for example, incorporating air pockets to increase its buoyancy. A neutrally buoyant microrobot would allow much finer weighing, as the magnetic forces would only compensate for the weight of the collected particle.<sup>[44]</sup> Second, the current system is limited to highly viscous fluids to slow down the system dynamics. Since the applied magnetic forces are similar to the effective weight of the microrobot, the velocities of the robot will approximately be the free-fall terminal velocity. Therefore, reducing the microrobot's effective weight and the applied forces would also allow the operation in less viscous media. Third, the stochastic nature of the collection operation can hinder the efficiency of the system. Visual tracking of particles during the collection process is challenging due to their occlusion by the microrobot. Therefore, a potential solution would be to analyze the distribution of particles when the microrobot is in a different location and use that information to plan an optimal position and angle for a future collection attempt. While the collection process

would remain stochastic, utilizing the distribution data could significantly improve the overall success rate. Finally, adaptive control techniques could be integrated to improve the system's performance under varying operating conditions.<sup>[45]</sup> A further consideration is the trade-off between using a rigid versus a soft microrobot. The primary limitation of a rigid microrobot, compared to soft microrobotic grippers, is its reduced ability to conform to and handle particles of varying shapes and sizes. However, rigid microrobots are easier to control and exhibit a higher magnetic moment than their similarly sized soft counterparts, enabling the manipulation of heavier particles.

To evaluate our system in comparison to other solutions, we analyze its throughput, autonomy, and potential applications. The presented system requires  $\approx 200$  s to sort each particle (0.005 samples per second). Although this throughput is lower than batch ( $>1000$  samples per second<sup>[13]</sup>) and tethered solutions (1–10 samples per second),<sup>[16]</sup> it is comparable with other untethered solutions for 3D sorting, which share the ability to operate in enclosed environments. For example, untethered soft magnetic microgrippers take 70–100 s per operation,<sup>[26–28]</sup> while collaborative magnetic grasping tools require around 150 s per operation. However, unlike these untethered systems, the approach proposed here operates fully autonomously, eliminating the need for human intervention in task execution. Furthermore, the system's adaptability to different media is demonstrated through the manipulation of a silica bead in a 2.5% w/v sodium CMC in water solution. The capability of the proposed system to perform sorting operations in this biocompatible aqueous solution opens the way for the sorting of encapsulated cell samples<sup>[46]</sup> of  $\approx 0.5$  mm in size. A particularly relevant use case for the proposed system could be the selective removal of dead or diseased samples to prevent contamination of healthy ones.

## 5. Experimental Section

**Microrobot, Media, and Passive Beads:** The microrobot was created by gluing a cylindrical magnet to a folded copper foil. The utilized magnet was a nickel-plated axially magnetized N50 neodymium magnet (remanence  $\|\mathbf{B}_r\| = 1.4$  T) of 0.75 mm diameter and 1 mm length (SuperMagnetMan, USA). The copper foil was 50  $\mu\text{m}$  thick and was cut to form a cylinder of 1.2 mm diameter and 2 mm length. Most experiments were performed in M1000 silicone oil (Carl Roth GmbH, Germany) with a density of 980 kg m<sup>-3</sup> and a viscosity of 1 Pa s. Additional experiments were performed in a 2.5% w/v solution of sodium CMC (Sigma-Aldrich, USA) in distilled water. The sorted passive beads were soda-lime glass beads (Carl Roth GmbH, Germany) with a diameter of 0.75–1.00 mm, and a density of 2500 kg m<sup>-3</sup>.

**Magnetic Actuation System:** The actuation system employed in this work consisted of nine VacoFlux-core coils placed at 30 mm from a common center.<sup>[47]</sup> Eight of them were on the corners of a cube, and the ninth was at the bottom. Nevertheless, for the experiments performed in this work, only the eight coils at the corners were used. Elmo Motion Control (Petach-Tikva, Israel) servo drives controlled the currents through the coils. The system was capable of generating magnetic fields of up to 100 mT and gradients of up to 1 T m<sup>-1</sup>. The system model,  $\mathcal{B}(\mathbf{P})$  and  $\mathcal{F}(\mathbf{P}, \mathbf{m})$ , was computed through finite elements analysis (see<sup>[47]</sup> for details) and was validated through empirical measurements performed with a Hall probe teslameter (Senis AG, Switzerland). The matrix norms are  $\|\mathcal{B}(\mathbf{P}_H)\| = 9.8 \text{ mT A}^{-1}$  and  $\|\mathcal{F}(\mathbf{P}_H)\| = 269 \mu\text{N A}^{-1}$  (for the used cylindrical magnet). A desktop computer connected to the cameras and coil drivers runs the control algorithm, composed of tracking, motion control [applying Equation (7)], and the actions scheduler (Algorithm 1). The

algorithm was implemented in a custom C++17 code on a Qt Creator 5.9 development environment, integrated code was generated by MATLAB 2022b to solve Equation (6) by finding the Moore–Penrose inverse matrix.

**Tracking:** The imaging system consists of two Grasshopper 3 (FLIR, USA) cameras imaging the system from the side and the top. The cameras operated at a resolution of 2048  $\times$  2048 pixels (corresponding to a pixel size of 10  $\mu\text{m}$ ) and an acquisition frequency of 10 Hz. We utilized an algorithm based on OpenCV 4.6 Canny edge detector to identify the position of the microrobot in each view. Finally, the 3D position was computed using a triangulation algorithm. A Luenberger observer was utilized to estimate the microrobot's velocity and to predict its position if tracking was temporarily lost.<sup>[48]</sup> For more details on the tracking algorithm, see Supporting Information.

## Supporting Information

Supporting Information is available from the Wiley Online Library or from the author.

## Acknowledgements

This work was supported by the European Commission under the Horizon Europe program under Grant no. 101070066 (RÉGO) and Grant no. 101070596 (euROBIN).

## Conflict of Interest

The authors declare no conflict of interest.

## Data Availability Statement

The data that support the findings of this study are available from the corresponding author upon reasonable request.

## Keywords

automation, magnetic actuation, microrobotics, planning, sorting

Received: February 18, 2025

Revised: June 19, 2025

Published online: August 5, 2025

- [1] M. Porta, G. Fantoni, P. Lambert, *CIRP J. Manuf. Sci. Technol.* **2010**, *3*, 185.
- [2] M. Sesen, G. Whyte, *Sci. Rep.* **2020**, *10*, 8736.
- [3] C. W. Shields IV, C. D. Reyes, G. P. López, *Lab Chip* **2015**, *15*, 1230.
- [4] P. Sajeesh, A. K. Sen, *Microfluid. Nanofluid.* **2014**, *17*, 1.
- [5] G. de Timary, C. J. Rousseau, L. Van Melderden, B. Scheid, *Lab Chip* **2023**, *23*, 659.
- [6] M. Islam, H. Brink, S. Blanche, C. DiPrete, T. Bongiorno, N. Stone, A. Liu, A. Philip, G. Wang, W. Lam, A. Alexeev, E. K. Waller, T. Sulchek, *Sci. Rep.* **2017**, *7*, 1997.
- [7] P. Li, Y. Ai, *Anal. Chem.* **2021**, *93*, 4108.
- [8] Y. Wei, X. Lu, J. Bao, S. Zhang, D. Wu, *Adv. Mater. Technol.* **2024**, 2301455.
- [9] A. Lefevre, M. Gauthier, P. Bourgeois, A. Frelet-Barrand, A. Bolepion, *Lab Chip* **2023**, *23*, 3683.
- [10] C. Lipp, L. Koebel, R. Loyon, A. Bolepion, L. Spehner, M. Gauthier, C. Borg, A. Bertsch, P. Renaud, *Lab Chip* **2023**, *23*, 3593.



- [11] H. Gu, Y. Chen, A. Lüders, T. Bertrand, E. Hanedan, P. Nielaba, C. Bechinger, B. J. Nelson, *Device*. **2024**, 2.
- [12] J. D. Adams, U. Kim, H. T. Soh, *Proc. Natl. Acad. Sci.* **2008**, 105, 18165.
- [13] Y. Shen, Y. Yalikun, Y. Tanaka, *Sens. Actuators, B* **2019**, 282, 268.
- [14] A. Diouf, F. Sadak, E. Gerena, A. Mannioui, D. Zizioli, I. Fassi, M. Boudaoud, G. Legnani, S. Haliyo, *J. Micro Bio Rob.* **2024**, 20, 3.
- [15] G. Fontana, S. Ruggeri, G. Legnani, I. Fassi, in *2018 Int. Conf. on Manipulation, Automation and Robotics at Small Scales (MARSS)*, IEEE **2018**, pp. 1–6.
- [16] M. Leveziel, W. Haouas, G. J. Laurent, M. Gauthier, R. Dahmouche, *Sci. Rob.* **2022**, 7, eabn4292.
- [17] J.-K. Heo, Kausthubharam, M. Jung, W. Kim, S. Jeong, D.-S. Song, Y.-J. Quan, J. H. Jeon, R. Ribeiro de Moura, S.-H. Ahn, *Int. J. Rob. Res.* **2024**, 43, 02783649241235215.
- [18] F. Nan, Z. Yan, *ACS Nano* **2020**, 14, 7602.
- [19] T. Xu, Y. Li, X. Han, L. Kan, J. Ren, L. Sun, Z. Diao, Y. Ji, P. Zhu, J. Xu, B. Ma, *Lab Chip* **2023**, 23, 125.
- [20] E. Gerena, S. Régnier, S. Haliyo, *IEEE Rob. Autom. Lett.* **2019**, 4, 647.
- [21] Q. M. Ta, C. C. Cheah, *IEEE/ASME Trans. Mechatron.* **2020**, 25, 1971.
- [22] F. N. Piñan Basualdo, A. Bolopion, M. Gauthier, P. Lambert, *Sci. Rob.* **2021**, 6, 52.
- [23] M. A. Rahman, N. Takahashi, K. F. Siliga, N. K. Ng, Z. Wang, A. T. Ohta, *Rob. Biomimetics* **2017**, 4, 1.
- [24] B. Ahmad, A. Barbot, G. Ulliac, A. Bolopion, *IEEE Rob. Autom. Lett.* **2023**, 8, 1675.
- [25] D. Loganathan, Y. Chaung, Y.-H. Lu, C.-H. Cheng, C.-Y. Chen, *Adv. Mater. Technol.* **2024**, 9, 2400292.
- [26] S. E. Chung, X. Dong, M. Sitti, *Lab Chip* **2015**, 15, 1667.
- [27] J. Zhang, O. Onaizah, K. Middleton, L. You, E. Diller, *IEEE Rob. Autom. Lett.* **2017**, 2, 835.
- [28] T. Xu, J. Zhang, M. Salehizadeh, O. Onaizah, E. Diller, *Sci. Rob.* **2019**, 4, eaav4494.
- [29] Y. Kantaros, B. V. Johnson, S. Chowdhury, D. J. Cappelleri, M. M. Zavlanos, *IEEE Trans. Rob.* **2018**, 34, 1472.
- [30] J. Jiang, L. Yang, B. Hao, T. Xu, X. Wu, L. Zhang, *IEEE Trans. Rob.* **2024**, 40.
- [31] F. N. Piñan Basualdo, S. Misra, *Adv. Intell. Syst.* **2023**, 5, 2300365.
- [32] Q. Wang, S. Yang, L. Zhang, *Nano-Micro Lett.* **2024**, 16, 40.
- [33] W. Jing, S. Chowdhury, M. Guix, J. Wang, Z. An, B. V. Johnson, D. J. Cappelleri, *IEEE Trans. Autom. Sci. Eng.* **2018**, 16, 518.
- [34] H. Xu, S. Wu, Y. Liu, X. Wang, A. K. Efremov, L. Wang, J. S. McCaskill, M. Medina-Sánchez, O. G. Schmidt, *Nat. Nanotechnol.* **2024**, 19, 494.
- [35] B. Ahmad, M. Gauthier, G. J. Laurent, A. Bolopion, *IEEE Trans. Rob.* **2022**, 38, 646.
- [36] K.-T. Yoon, S.-R. Park, Y.-M. Choi, *Meas. Sci. Technol.* **2020**, 32, 015905.
- [37] B. E. Dolata, R. N. Zia, *J. Fluid Mech.* **2021**, 910, A22.
- [38] M. P. Kummer, J. J. Abbott, B. E. Kratochvil, R. Borer, A. Sengul, B. J. Nelson, *IEEE Trans. Rob.* **2010**, 26, 1006.
- [39] F. N. Piñan Basualdo, O. Stéphan, A. Bolopion, M. Gauthier, P. Lambert, *IEEE/ASME Trans. Mechatron.* **2023**.
- [40] J. J. Kuffner, S. M. LaValle, in *Proceedings 2000 ICRA. Millennium Conf. IEEE Int. Conf. on Robotics and Automation. Symposia Proceedings (Cat. No. 00CH37065)*, Vol. 2, IEEE **2000**, pp. 995–1001.
- [41] F. N. Fritsch, R. E. Carlson, *SIAM J. Numer. Anal.* **1980**, 17, 238.
- [42] X. H. Yang, W. L. Zhu, *Cellulose* **2007**, 14, 409.
- [43] X. Shen, P. E. Arratia, *Phys. Rev. Lett.* **2011**, 106, 208101.
- [44] E. Diller, J. Giltinan, M. Sitti, *Int. J. Rob. Res.* **2013**, 32, 614.
- [45] M. Sallam, M. A. Shamseldin, F. Ficuciello, *Front. Rob. AI* **2024**, 11, 1439427.
- [46] X. Peng, Ž. Janićijević, S. Lemm, M. Laube, J. Pietzsch, M. Bachmann, L. Baraban, *Biotechnol. J.* **2023**, 18, 2200365.
- [47] F. Ongaro, S. Pane, S. Scheggi, S. Misra, *IEEE Trans. Rob.* **2018**, 35, 174.
- [48] D. Luenberger, *IEEE Trans. Autom. Control* **1966**, 11, 190.